Research Article

Roberto Fallica*

Beyond grayscale lithography: inherently three-dimensional patterning by Talbot effect

https://doi.org/10.1515/aot-2019-0005
Received January 10, 2019; accepted April 23, 2019; previously published online May 23, 2019

Abstract: There are a growing number of applications where three-dimensional patterning is needed for the fabrication of micro- and nanostructures. Thus far, grayscale lithography is the main technique for obtaining a thickness gradient in a resist material that is exploited for pattern transfer by anisotropic etch. However, truly three-dimensional structures can only be produced by unconventional lithography methods such as direct laser writing, focused ion beam electrodeposition, colloidal sphere lithography, and tilted multiple-pass projection lithography, but at the cost of remarkable complexity and lengthiness. In this work, the three-dimensional shape of light, which is formed by Talbot effect diffraction, was exploited to produce inherently three-dimensional patterns in a photosensitive polymer. Using light in the soft X-ray wavelength, periodic three-dimensional structures of lateral period 600 nm were obtained. The position at which the sample has to be located to be in the Fresnel regime was simulated using an analytical implementation of the Fresnel integrals approach. Exploiting the light shape forming in diffraction effects thus enables the patterning of high-resolution three-dimensional nanostructures over a large area and with a single exposure pass – which would be otherwise impossible with conventional lithographic methods.

Keywords: 3D lithography; grayscale lithography; soft X-rays; Talbot.

1 Introduction

Conventional lithography is the mainstream technique for producing two-dimensional geometries onto a resist material, which is then used as a sacrificial layer for pattern transfer to underlying layers (such as monocrystalline silicon or metal hard mask) by anisotropic etch. The pattern produced in the resist by conventional lithography is binary; in other words, photoresist is either completely removed or completely preserved after development. Meanwhile, patterning by grayscale lithography is fundamentally different because it aims at achieving a continuous variation of resist thickness. This thickness gradient is then used for the fabrication of a variety of micro- and nanostructures, such as micro-optical interconnects [1], kinoform lenses for X-ray focusing [2], microfluidics channels of variable geometry [3], blazed gratings [4], micro-electromechanical devices [5], optical diffusers [6], and biomimetic structures [7]. The key enablers to grayscale lithography have been the ability to control the amount of energy deposited (i.e. the exposure dose) across the sample and within the pattern, the availability of low-contrast (photo)resist materials and development processes, and the use of an appropriate transfer function. These technological advances made it possible to achieve an unprecedented control of the remaining resist thickness gradient and surface morphology. As a result, grayscale lithography has been hugely successful in opening new possibilities and accelerating the production of novel nano- and microstructures.

There are traditionally two main ways of achieving dose control in grayscale lithography. The first is by using a grayscale mask of varying transmissivity in combination with a projection lithographic source (such as optical [1, 8] or ion [9]), and the other way is by use of a raster scan exposure tool where the dose is controlled *on the fly*, for example by tuning the dwell time of an electron beam [7]. In the former case, additional time is required to preliminarily prepare an *ad hoc* graytone mask. The latter case is instead a maskless method, which brings the advantage in terms of versatility; however, it requires a longer setup time to calibrate the process parameters. Nevertheless, it has been demonstrated that accurate control of the thickness, sidewall angle, and shrinkage of the resist in maskless grayscale lithography is possible [10].

***Corresponding author: Roberto Fallica,** Paul Scherrer Institut, 5232 Villigen PSI, Switzerland, e-mail: roberto.fallica@imec.be.
https://orcid.org/0000-0003-4523-9624

All the grayscale lithography methods discussed thus far are still limited to producing a surface owing to the unavoidable fact that only the intensity, but not the shape of the aerial image, is changing during exposure. Instead, truly three-dimensional micro- and nanostructures can only be fabricated by going beyond grayscale lithography, for example by use of raster-scan techniques that exploit all three axes (such as direct laser writing [11] and focused ion beam electrodeposition [12]), or by unconventional fabrication methods such as colloidal assembly of microspheres [13], polychromatic electron beam lithography [14], multiple-pass tilted ultraviolet [15], and X-ray [16] lithography. All these works demonstrate remarkable ingenuity but have a huge drawback of significantly increasing the process complexity and time.

The main limitation when building a three-dimensional structure is the fact that the aerial image incident on the resist has a two-dimensional shape. The aerial image can be tuned for intensity across two dimensions, thus giving rise to grayscale patterns, or it can be rasterized, or tilted, or defocused to form three-dimensional patterns as in the examples discussed in the previous paragraph. There are, however, other ways to work around this limitation by exploiting wave effects and give shape to an *inherently* three-dimensional aerial image. An illustrative example is the case of two-beam interference lithography of arrays of dense alternating lines and spaces; here, the aerial image extends in three dimensions and is z-invariant, thus bringing the advantage of unlimited depth of focus for patterning of thin films [17]. Diffraction effects of light passing through a mask with apertures of size comparable to its wavelength give rise to much more complex and three-dimensionally shaped aerial images. Optical soft X-ray lithography has been exploiting Talbot effects to achieve high-throughput, large-area patterning by means of the self-imaging and demagnification of the mask in the achromatic regime [17]. Holographic lithography is another way to achieve the fabrication of complex, fully three-dimensional patterns, as has been demonstrated in experiments [18] and simulations [19]. In this paper, this concept is extended, and the unique shape of the aerial image formed by the Talbot effect of soft X-rays in the Fresnel regime is exploited to produce inherently three-dimensional patterns onto a thick photosensitive polymer. The implementation of this technique demonstrates that novel high-resolution patterning methods based on versatile aerial image shaping are possible and can be implemented on large areas.

2 Experimental details

Linearly polarized soft X-ray light was generated in the XIL beamline of the Swiss Light Source synchrotron. Light of two wavelengths was used: 13.5 nm (92 eV) and 7.75 nm (160 eV), in both cases with spectral resolution $\Delta\lambda/\lambda \approx 0.04$. Beam monitor was used to measure the flux in these two conditions, which was about 30 mW/cm^2. As a result, the exposure dose was determined by the product of flux and exposure time. In this work, the following conditions have been used for the patterning: 100 mJ/cm^2 for low-dose condition (13.5 nm), 150 mJ/cm^2 for high-dose condition (13.5 nm), and 300 mJ/cm^2 for 7.75-nm wavelength. It is important to note, however, that these incident dose values are not directly comparable with those normally used in soft X-ray lithography owing to the mask efficiency that changes the amount of light actually transferred to the sample. This choice of wavelengths was dictated by other constraints that will be discussed later in this section.

Exposures were carried out using a lithography tool consisting of a vacuum chamber – preliminarily evacuated to a pressure of 10^{-6} mbar or better – where the sample could be positioned via a three-axis motorized stage. The tool was equipped with a diffraction transmission mask; the mask-to-sample distance was controlled across a range of several millimeters with a resolution of about 5 μm. To exploit Talbot effect diffraction, the mask consisted of a suspended silicon nitride membrane on which an absorber film of chromium was previously patterned as an array of circular holes of diameter 150 nm and pitch 600 nm over a total area of (0.575 mm)^2.

Poly(methyl methacrylate), PMMA, was used as photoresist in positive-tone mode and was chosen owing to its photosensitivity to a broad range of wavelengths. A commercially available PMMA solution of molecular weight 600k cast at 8% concentration in ethyl lactate was spin coated at 1000 rpm for 2 min on a blank 4-in-diameter monocrystalline silicon wafer. The resulting thickness before exposure, measured by single-point visible-light reflectometry in normal incidence, was ≈6.6 μm. A post-application bake of the samples was carried out on a hot plate at 140°C for 120 s in air to evaporate the remaining solvent from the film. After exposure, the samples were developed in methyl isobutyl ketone diluted in three parts of isopropyl alcohol for 30 s at room temperature, followed by rinse for 30 s in isopropyl alcohol at room temperature.

In the design of this experiment, the choice of wavelengths in the soft X-ray was dictated by three key factors: the goal of demonstrating higher patterning resolution in comparison to previous studies, the penetration depth of light in the material, and the geometrical constraints on the mask-to-sample distance, which ensure that the aerial image is being sampled in the Fresnel regime. For what concerns resolution, previous studies reported the patterning of Talbot carpet using coherent light of wavelength ranging from the visible (632.8 nm, HeNe laser) [20] to the extreme ultraviolet (EUV, 13.5 nm) [21]. EUV and shorter wavelengths are especially interesting from the technological point of view, as these are the wavelengths of choice for next-generation optical lithography [22]. Notably, absorption of light in matter is much more intense in EUV than it is in other wavelengths, as illustrated in Figure 1, which shows the optical attenuation length of light from 14 to 4 nm wavelength in PMMA. The attenuation length is relevant due to its consequence on the volume of the three-dimensional aerial image that it is possible to record along the depth of the resist. For instance, patterning PMMA with light in the EUV wavelength, we expect that there will

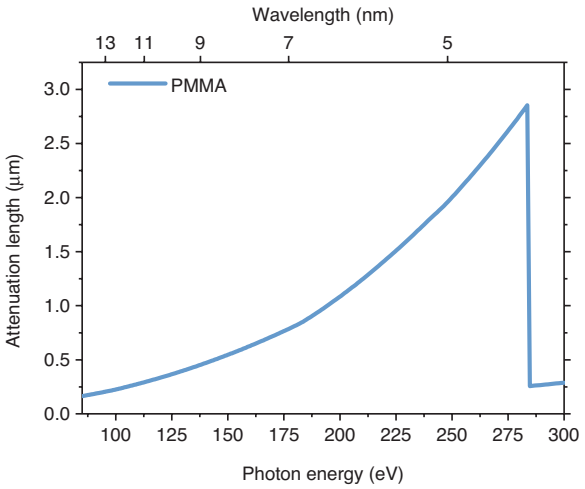

Figure 1: Plot of the attenuation length of light in PMMA in the soft X-ray range, from data obtained from the CXRO database.[a] The EUV wavelength is at 13.5 nm, where absorption is considerably higher than elsewhere. [a]http://henke.lbl.gov/optical_constants/ and B. L. Henke, E. M. Gullikson and J.C. Davis, Atomic Data and Nuclear Data Tables 54, 181 (1993).

be enough light to clear the photoresist up to about 1.5 μm depth, whereas 7.75-nm-wavelength light is expected to reach twice as deep in the photoresist. This observation also justifies why the coating thickness of PMMA was chosen to be much larger than the attenuation length and why a positive-tone process had to be used. In a positive-tone processing, the exposed volume of PMMA becomes more soluble to the developer and gets removed; however, the development begins from the top surface of PMMA and proceeds as deep in the resist as the liquid developer can find a percolation path. According to Figure 1, a shorter wavelength (of about 5 nm) would be more effective in sampling a deeper aerial image; however, practical considerations prevent the use of shorter wavelengths for lithography in this tool.

The Talbot effect is a coherent diffraction phenomenon [23] where monochromatic light passing through the apertures of a mask generates self-images of the mask at periodic distances, and demagnified replicas at fractional distances [21, 24]. The physical description of the diffraction regimes (monochromatic and achromatic) depends on the distance from the source aperture and on the non-perfect monochromaticity of the light and it has been extensively described in the literature. To our purpose, it should be noted that the aerial image is three-dimensional only in the region of space when the Fresnel number, N_F, is equal to or smaller than unity:

$$N_F = \frac{a^2}{z\lambda} \leq 1,$$

where a is the size of the aperture in the mask, z is the distance from the mask, and λ is the wavelength of light. With a mask-to-sample distance of 0.1 mm and aperture size of 200 nm, we are in such condition ($N_F = 0.03$). In the scope of this work, the wafer-to-mask distance is therefore constrained to lie in a specific region of space so as exploit the fully three-dimensional aerial image. This region is dictated by two optical constraints: the monochromatic Talbot distance and the achromatic Talbot distance. When the sample is too far away from the mask (above the achromatic Talbot distance), we are in the Fraunhofer regime where the aerial image becomes z-invariant, a condition used in conventional non-grayscale patterning. Meanwhile, when the sample-to-mask distance is reduced below the monochromatic distance, we are in near-field regime where complex Talbot "carpets" are formed. In this region of space, the aerial intensity changes with very high resolution, a condition that has been used to achieve spatial frequency multiplication in two-dimensional patterning [21]; however, it is not considered ideal for three-dimensional patterning. Moreover, controlling the position of the mask is not straightforward when the gap distance is only few microns from the sample. Therefore, for the purpose of this work, the best aerial image geometry is obtained in the Fresnel regime. The Talbot distances have been calculated for the setup geometry and are summarized in Table 1.

The morphology of the patterned samples was inspected using top-down scanning electron microscopy (SEM) at 2-keV voltage acceleration. Selected samples were also inspected in cross section, by cleaving the silicon substrate along a crystalline plane in order to estimate the penetration depth and profile of the remaining resist. To avoid electric charging and deformations of the PMMA due to the damage induced by highly energetic electrons in the SEM, an electrically conductive thin film of chromium (5 nm) was deposited on top of the samples by thermal evaporation prior to SEM inspection.

3 Simulation

The mathematical expression describing the Fresnel diffraction of light passing through an array of apertures can be solved by use of two-dimensional fast Fourier transform. In the case of a square array of apertures, the exact analytical calculation of light intensity at any distance z can be done using Fresnel cosine and sine integrals. A numerical implementation of this analytical solution by use of the Fresnel integrals approach for a finite square

Table 1: Summary of optical conditions used: wavelength, λ, period on mask, p, aperture, a, and spectral bandwidth of the beamline, $\Delta\lambda$.

Wavelength λ (nm)	Period on mask p (nm)	Mask aperture a (nm)	Spectral bandwidth $\Delta\lambda$ (nm)	Monochromatic distance Z_T (μm)	Achromatic distance Z_A (μm)	Maximum distance Z_{max} (μm)
13.5	600	150	0.54	53.3	1333	2222
7.75	600	150	0.31	92.9	2323	3871

From these three parameters, the monochromatic Talbot distance Z_T, the achromatic Talbot distance Z_A, and the maximum exposed distance Z_{max} are calculated.

array of apertures was recently reported [25]. This algorithm was coded in MATLAB and can be tailored to any geometry by dialing in the pitch and size of the apertures, and the size of the array of apertures. The algorithm provides an exact solution of the aerial image intensity for a two-dimensional slice at fixed z distance from the mask and parallel to it, in the simplifying assumption of an infinitely thin mask. In this work, the values used were consistent with the experiment: aperture size 150 nm, aperture pitch 600 nm, and mask-to-sample distance variable from 180 to 220 μm in steps of 5 μm. The total number of apertures heavily impacts the computational time and, for this reason, it was set to a 20×20 array. This number of apertures was sufficiently large to detect and avoid edge effect from the mask, as shown in Figure 2, which shows the calculation of the intensity of 13.5-nm-wavelength light in a plane at distance $z = 80$ μm from a mask having a 20×20 array of apertures of pitch 600 nm and size 150 nm. The simulation proves that the aperture array chosen was large enough so that edge effects do not impact the center of the simulated area. Finally, it should be noted that owing to the symmetry of the system (two axis), only a quarter of the area was computed.

To generate a three-dimensional aerial image intensity, the algorithm is evaluated at discrete values of z in the range of interest and the resulting three-dimensional intensity plot was determined by linear interpolation.

4 Results

Just as in any lithographic process, the fabrication of inherently three-dimensional patterns consists in turning an aerial image into a latent resist image: the light-induced scissions reduce the molecular weight and increase the solubility of PMMA. In this work, the lithography processing is the same as that of conventional lithography but the Talbot effect is exploited to produce an inherently three-dimensional aerial image. Moreover, as the development begun from the top (open) surface of the film and proceeded downwards, only those parts of the film accessible to the developer could be effectively dissolved and removed.

Initially, a mask-to-wafer distance $z = 1000$ μm was used; the resulting pattern was two dimensional and consisted of a self-image of the mask (Figure 3). As the intensity of soft X-rays decays quickly in matter, a sizeable reduction in light intensity is expected as one looks deeper in the resist (e.g. along the cross section of PMMA). The exposure of PMMA at 13.5-nm wavelength was expected to result in the shallowest penetration depth.

As the mask distance was reduced to 200 μm (into the Fresnel regime), light received by the PMMA layer produced a depth-dependent profile and a complex interference pattern, which becomes evident in the SEM picture after development (Figure 4A). To a first approximation,

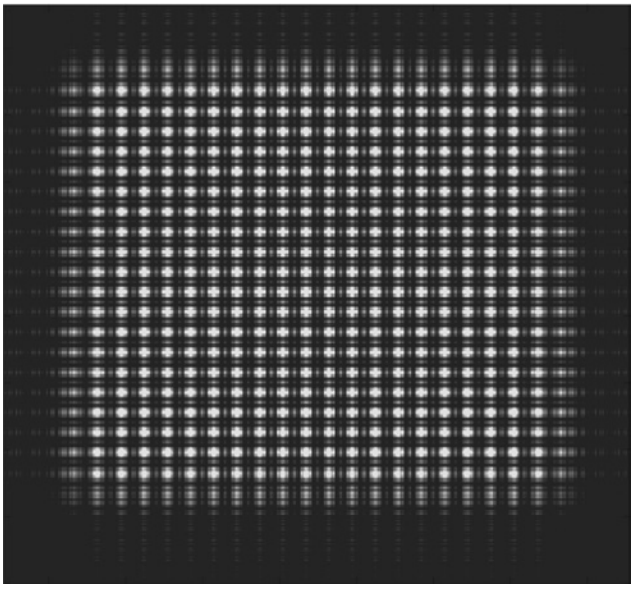

Figure 2: Aerial image intensity calculated using the numerical algorithm based on the Fresnel integrals due to the Talbot effect on a plane parallel to the mask and at a distance $z = 80$ μm from it; the mask consists of an array of 20×20 apertures of pitch 600 nm and size 150 nm, and the light wavelength was 13.5 nm.

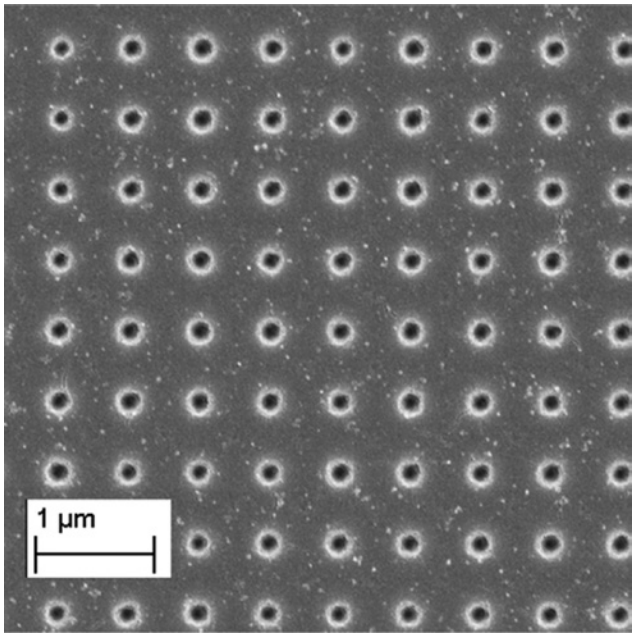

Figure 3: Scanning electron micrographs of PMMA film after exposure to 13.5-nm light and development at a relatively long distance from the mask (1000 μm). The pattern is simply the self-image of the mask.

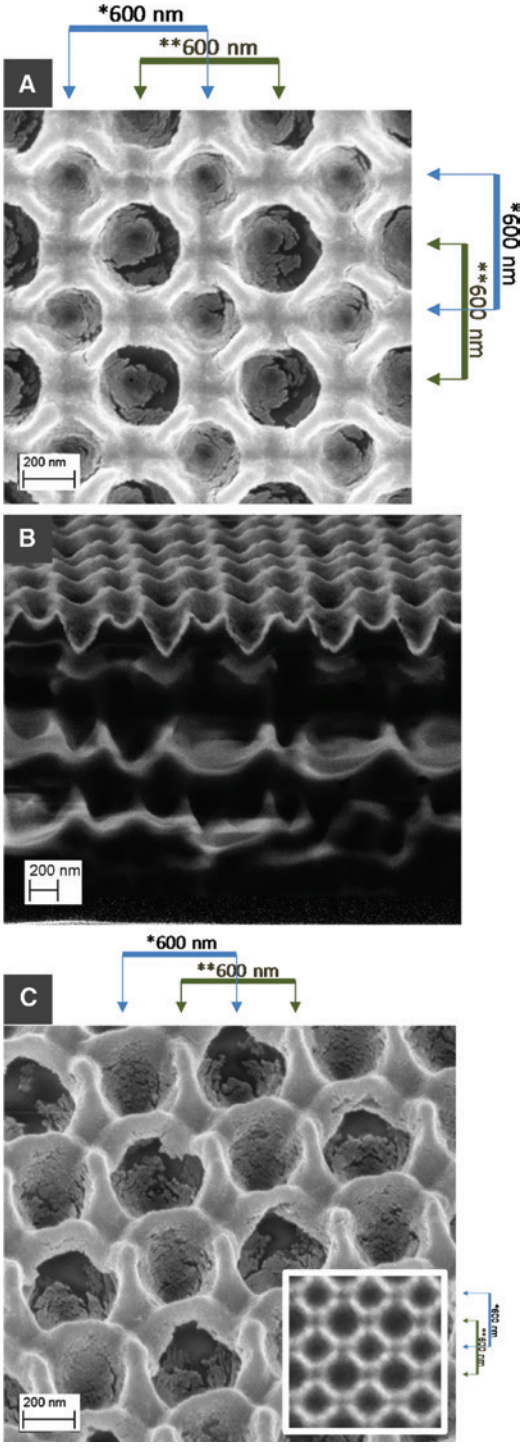

Figure 4: Scanning electron micrographs of PMMA patterned by three-dimensional aerial images obtained by the Talbot effect in the EUV wavelength. Diffraction effects (having same periodicity but phase shift π along x and y) combine to generate three-dimensional aerial images that expose the PMMA film to an egg carton shape. Low-exposure-dose top-down view at 0° (A), low-exposure-dose cross section at 80° (B), high-exposure-dose tilted view at 70° (C), and high-exposure-dose top-down view (C, inset). The blue and green arrows indicate the position of the two repeating patterns of 600-nm period, i.e. the self-images of the mask.

the amount of dissolution switch in a photoresist during lithography is proportional to the intensity of light. In the picture, it is possible to identify at least two superimposed self-images of the mask, one with higher intensity and another with weaker intensity and phase shifted by π along X and Y. Additionally, weaker diffraction orders were also present at $\pi/2$. The cross-sectional profile (Figure 4B) of that pattern indicates that the light was so heavily absorbed that, beyond 400-nm depth, the exposure of the PMMA was not enough to make it soluble. Tuning the amount of energy deposited while keeping the same z distance, it was possible to shift the dissolution threshold of the material and obtain a three-dimensional pattern resembling an egg carton (tilted view, Figure 4C).

When the wavelength was changed to 7.75 nm, a similar result as in the 13.5-nm exposure was obtained, with the top-down view (Figure 5A) showing that the aerial image was a combination of several diffraction orders. The tilted view (Figure 5B) better illustrates the three-dimensional shape of these nanopatterns that resemble flower blossoms. However, the side view in cross section (Figure 5C) clearly indicates how the three-dimensional aerial image extended farther than in the case of 13.5-nm exposure. The result was an array of dimples, ≈ 2 µm deep and slightly tapered due to the light absorption, dug in the PMMA. Notably, it is also possible to detect additional other latent images at depth ≥ 3 µm in the resist. These brighter regions of resist, buried deeper in the film, demonstrate that the PMMA had been exposed to enough light to trigger the scission of the polymer chain and therefore had lower molecular weight than the rest of the material (appearing brighter under the SEM beam). Still, the continuous layer of unexposed PMMA, which capped these exposed areas, prevented the developer from reaching and dissolving away these deep buried regions of photoresist.

The aerial image formed by the diffraction of light when it propagates several tens of micrometers from the mask was simulated with the numerical algorithm. The punctual value of intensity of light of 7.75 nm wavelength was calculated in an array of $3000 \times 3000 \times 100$ points corresponding to a (x, y, z) volume of dimensions 12 µm (x), 12 µm (y), and 200 µm (z), respectively. Assuming that the solubility of the PMMA is proportional to the amount of light received, the remaining resist after development can also be approximated reasonably well by applying a constant threshold to the solubility. The aerial image intensity shows a relatively complex shape in three-dimensional space (because most regions have non-zero value). A meaningful representation of the aerial image intensity for lithographic purposes is given in Figure 6, which shows the regions of space where its normalized intensity

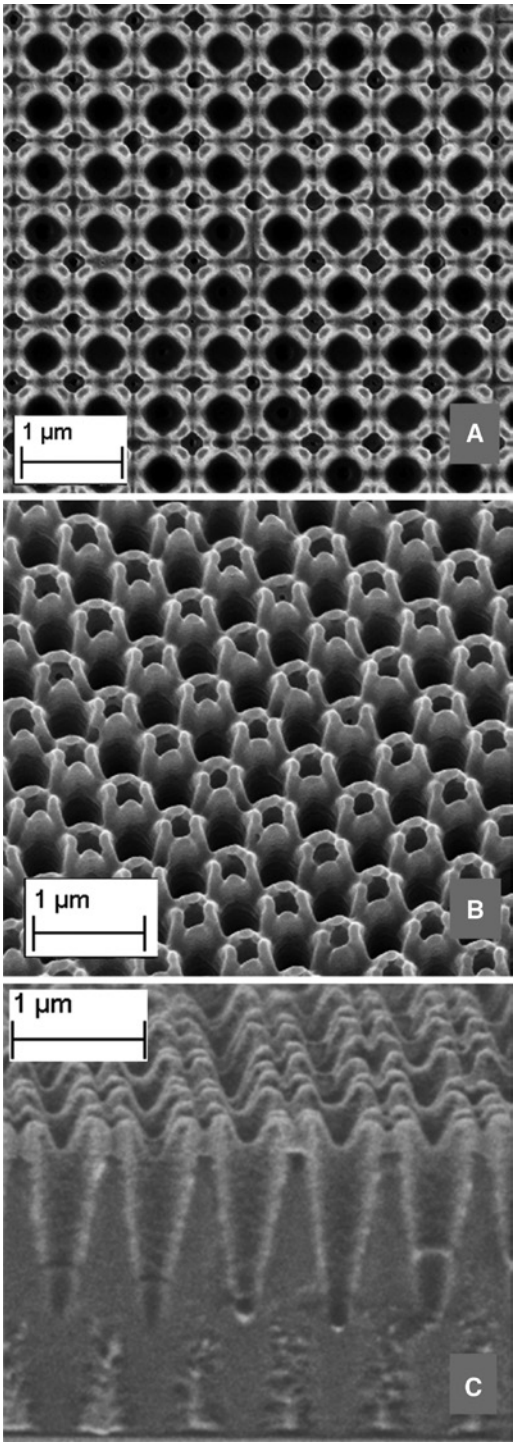

Figure 5: Scanning electron micrographs of PMMA patterned by three-dimensional aerial images obtained by the Talbot effect with light of 7.75-nm wavelength. Top-down view at 0° (A), tilted view at 70° (B), and cross-section view at 80° (C) show the dense array of dimples of 600-nm period. According to the cross-section view (C), light of this wavelength reached the PMMA up to 3 µm and deeper, where parts of exposed but undeveloped material are barely visible as brighter regions. The tilted perspective (B) demonstrates the blossom-like pattern that can be achieved by exploiting the aerial image effects.

was equal to or above a 0.7 threshold, as seen on a section plane parallel to xz at $y=0$ (one of the two axis of symmetry). The figure clarifies how the regions of high enough intensity (≥0.7) of the aerial image had the shape of two arrays of periodic ellipsoids with the same periodicity but not z-invariant. The variation of shape along z is a consequence of the finite bandwidth of the light and of the edge effects at the mask. The center of each ellipsoid was, on the xy plane, located in either of two possible positions, which differ only by a π phase – in agreement with the image recorded in the resist by the solubility threshold. To clarify how the aerial image intensity of Figure 6 relates with the patterned photoresist of the previous section, a few considerations are needed. In the experiment, the layer of PMMA is located at a given distance z_e from the mask and because of its finite thickness t, it extends in a region of space that goes from $z=z_e$ to $z=z_e+t$. From Figure 6, it is possible to see that for any location in z, the surface of the PMMA film is exposed somewhere. As a result, there is always an exposed part on the film surface that allows for the development process to continue removing the photoresist throughout the depth of the material (provided that the dose is above threshold). Finally, note that Figure 6 is an aerial image in space, and it does not take into account the optical absorption of matter. The effect of optical absorption is, as mentioned previously, to reduce and narrow the width of the ellipsoidal shapes of PMMA that become cleared in the development.

The fast and large-area fabrication of high-resolution patterns is of interest for applications such as energy dispersive optical elements. The periodicity of 600 nm in both in-plane directions x and y of the patterns obtained

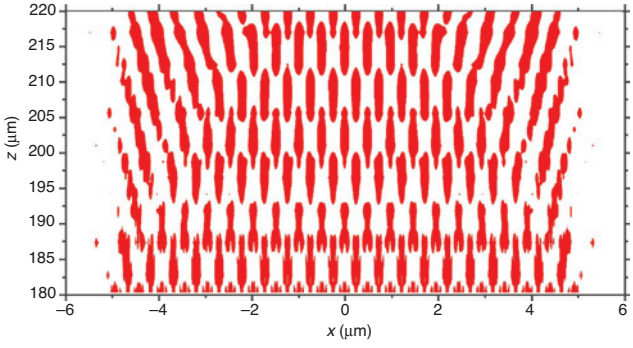

Figure 6: Simulation of the aerial image of a 7.75-nm-wavelength light passing through a mask of 600 nm pitch and 150 nm aperture, using the Fresnel integrals approach. The view is a cross section along the xz plane at $y=0$ and shows how the Talbot effect gives rise to a complex diffraction pattern that is not z-invariant. The ellipsoids represent volumes of space (at distance z from the mask) where the relative light intensity was equal to or above a given threshold of 0.7.

Figure 7: Photograph of an 8×8 array of three-dimensional PMMA patterns, each (0.575 mm)² in area, obtained by the Talbot effect when illuminated to unpolarized white light. Owing to the periodicity of the structures, the element shows optically dispersive behavior in the visible.

in this work with Talbot lithography is especially suitable for applications in the visible. Figure 7 shows a visible-light photograph of the three-dimensional arrays illuminated by white unpolarized light. The reflection of light from unpatterned areas of PMMA is almost negligible. Instead, the three-dimensional arrays of lateral size ≈ (0.575 mm)² are clearly visible and reflect brightly. The position on wafer of each array is shifted by ≈ 1.5 mm from its neighbors. White light from the source is reflected and refracted at different angles depending on the wavelength and, as a result, the three-dimensional arrays appear to the observer in different colors, effectively working as optically dispersive elements. Future work will be devoted to the evaluation of the efficiency of these three-dimensional arrays in comparison to traditional geometry.

5 Conclusions

In this work, light diffraction due to the Talbot effect has been exploited to generate inherently three-dimensional structures in a photosensitive polymer in a way that would be otherwise impossible by conventional methods. The main advantage of this technique is the simplicity and speed of the processing and versatility because any positive-tone photoresist can be used for the purpose. The Talbot effect can be exploited as long as the mask-to-wafer distance is carefully controlled. Only a single exposure step is needed, which greatly reduces the complexity. As a result, large-area patterning at very high resolution can be obtained with an exposure time of few seconds. This result is promising to achieve fast and inexpensive nanofabrication of large photonic crystals for applications in the visible. The design of experiment is simplified by the use of a numerical algorithm to estimate the position along z where the Talbot effect produces the desired aerial image. Exposure can then be carried out by accurately positioning the sample by using an interferometric positioner. In this way, it has been demonstrated that the three-dimensional aerial image can be sampled and recorded in the resist.

Further research is needed to investigate the performance of photonic crystals fabricated by this route, for instance by analyzing the efficiency and angular dependence of the incident angle. Additional investigation could also extend this concept to use light of wavelength shorter than 7.75 nm, where the photoabsorptivity of organic materials is low enough that patterning of several-micrometer-deep three-dimensional structures will become possible. Lithography at these wavelengths is challenging because the energy required to expose such a large volume of material becomes spread across larger and larger volumes, increasing the exposure time; moreover, there is a lack of sources capable of producing photons in that energy and high flux. Naturally, using a shorter wavelength will affect the Fresnel number and therefore a different mask geometry (smaller aperture size) will have to be adopted to keep the achromatic distance within reasonable limits, lest the loss of the three-dimensionality of the aerial image.

Acknowledgments: The contributions of Michaela Vockenhuber, Markus Kropf, and Iacopo Mochi (Paul Scherrer Institute) are kindly acknowledged. Part of this work was performed at the Swiss Light Source of the Paul Scherrer Institute.

References

[1] T. Dillon, M. Zablocki, J. Murakowski and D. Prather, Proc. SPIE 6923, 69233B (2008).
[2] J. Vila-Comamala, S. Gorelick, V. A. Guzenko and C. David, J. Vacuum Sci. Technol. B 29, 06F301 (2011).
[3] J. Atencia, S. Barnes, J. Douglas, M. Meacham and L. E. Locascio, Lab Chip 7, 1567 (2007).
[4] R. Fallica, R. Kirchner, H. Schift and Y. Ekinci, Microelectr. Eng. 177, 1 (2017)
[5] C. M. Waits, B. Morgan, M. Kastantin and R. Ghodssi, Sens. Actuators A 119, 245 (2005).
[6] P. P. Naulleau, J. A. Liddle, F. Salmassi, E. H. Anderson and E. M. Gullikson, Appl. Opt. 43, 5323 (2004).

[7] R. Kirchner, V. A. Guzenko, M. Rohn, E. Sonntag, M. Mühlberger, et al., Microelectron. Eng. 141, 107 (2015).
[8] H. Mekaru, Micromachines 6, 252 (2015).
[9] S. Hirscher, R. Kaesmaier, W. -D. Domke, A. Wolter, H. Loeschner, et al., Microelectron. Eng. 57, 517 (2001).
[10] C. Kaspar, J. Butschke, M. Irmscher, S. Martens, H. Sailer, et al., J. Vacuum Sci. Technol. B 35, 06G501 (2017).
[11] M. Deubel, G. von Freymann, M. Wegener, S. Pereira, K. Busch, et al., Nat. Mater. 3, 444 (2004).
[12] G. Seniutinas, A. Balčytis, I. Reklaitis, F. Chen, J. Davis, et al., Nanophotonics 6, 923 (2017)
[13] Y. A. Vlasov, X. -Z. Bo, J. C. Sturm and D. J. Norris, Nature 414, 289 (2001).
[14] Y. Matsubara, J. Taniguchi and I. Miyamoto, Jap. J. Appl. Phys. 45, 5538 (2006).
[15] J. B. Lee, K. -H. Choi and K. Yoo, Micromachines 6, 1 (2015).
[16] F. Romanato, L. Businaro, L. Vaccari, S. Cabrini, P. Candeloro, et al., Microelectron. Eng. 479, 67 (2003).
[17] H. Solak, J. Phys. D Appl. Phys. 39, R171 (2006).
[18] Y. V. Miklyaev, D. C. Meisel, A. Blanco, G. Freymann, K. Busch, et al., Appl. Phys. Lett. 82, 1284–1286 (2003).
[19] R. C. Rumpf and E. G. Johnson, J. Opt. Soc. Am. A 21, 1703 (2004).
[20] H. Kim, S. Danylyuk, W. S. Brocklesby and L. Juschkin, J. Opt. Soc. Korea 20, 245 (2016).
[21] H. Kim, W. Li, S. Danylyuk, W. S. Brocklesby, M. C. Marconi, et al., J. Phys. D Appl. Phys. 48, 375101 (2015).
[22] R. M. M. Hasan and X. Luo, Nanomanufact. Metrol. 1, 67 (2018).
[23] H.F. Talbot, Philos. Mag. Ser. 39, 401 (1836).
[24] B. Besold and N. Lindlein, Opt. Eng. 36, 1099 (1997).
[25] A. A. Goloborodko, Optik 127, 4478 (2016).